scientific reports

OPEN

Rapid inactivation of bacteria by MoS_2/g-C_3N_4 nanohybrid structures driven by visible light

Ping Li[1,2,4], Yuting Zhai[1,2,3,4], Jiaxiu Liu[1,2], Yangru Dai[1,2,3], Daohao Li[3] & Shuchao Zhang[1,2,3]✉

Photocatalytic water disinfection is a cutting-edge strategy for effectively sterilizing water in a cost-effective and environmentally friendly manner. A 2D/2D MoS_2/g-C_3N_4 heterojunction photocatalyst was specifically designed to improve performance by enhancing the charge separation and reducing the photogenerated carrier loading rate. When exposed to visible light, electron and hole pairs generated on the surface of the heterojunction interacted with O_2 and H_2O in the environment; this facilitated the production of exogenous reactive oxygen species (ROS) that effectively eliminated the bacteria. With this optimized structure, *E. coli* and *S. aureus* were completely inactivated in 20 and 30 min, respectively, under white LED irradiation.

Keywords MoS_2, g-C_3N_4, Heterostructure, Bacterial inactivation, Photocatalysis

In recent decades, water pollution has become increasingly severe globally, and pathogenic microorganisms (fungi, bacteria, viruses, etc.) in water can cause waterborne infectious diseases, which seriously jeopardize people's health[1]. Traditional methods of water pollution treatment, such as ultraviolet irradiation, chemical disinfection (e.g. chlorine (Cl_2), ozone (O_3), and chloramines (H_2NCl)), and membrane filtration, have certain limitations[2]. Problems such as high energy consumption, high production costs, long preparation times, and secondary pollution are common, limiting their large-scale application. Therefore, a new water purification method that is low cost, efficient and environmentally friendly needs to be developed. Photocatalytic technology is widely utilized because of its advantages, such as low energy consumption, high stability, high efficiency, absence of secondary waste generation, and environmental friendliness[3]. It is considered a novel method that can supplant traditional water purification strategies. Photocatalytic technology interacts with ambient H_2O and O_2 to produce exogenous reactive oxygen species (ROS), including singlet oxygen ($^1O_2$), hydroxyl radicals (·OH), and superoxide radicals ($\cdot O_2^-$); these species can disrupt the proteins and lipids on the bacterial membrane, leading to bacterial inactivation[4]. Furthermore, ·OH and $\cdot O_2^-$ can destroy the pathogenic microorganisms by attacking the cell membranes through advanced oxidative processes; this causes leakage of the intracellular substances or DNA destruction, thereby resulting in disinfection and sterilization[5]. To date, a variety of semiconductor materials have been developed for photocatalytic water purification and include TiO_2[6], g-C_3N_4[7], and ZnO[8]. However, the photocatalysts used in the aforementioned work suffer from low photocatalytic stability[9], low spectral utilization efficiency[10,11], and low bactericidal efficiency[12]. Therefore, designing a photocatalyst with high catalytic stability, high solar energy utilization, and high bactericidal efficiency is crucial.

As a two-dimensional metal-free semiconductor with a unique structure, g-C_3N_4 has become popular for research because of its low cost, nontoxicity, simple preparation and strong photoreduction ability[13]. However, the inherent narrow spectral response and high recombination rate of the photogenerated carriers severely limit the photocatalytic performance of g-C_3N_4. To address this issue, researchers have made significant efforts and discovered that coupling g-C_3N_4 with suitable bandgap semiconductors to construct heterostructures can broaden the visible light absorption range of g-C_3N_4-based composites and effectively accelerate the interfacial charge separation, thus increasing photocatalytic efficiency[14]. Examples include TiO_2/g-C_3N_4[15], Bi_2MoO_6/g-C_3N_4[16] and $BiFeO_3$/g-C_3N_4[17]. These heterostructures exhibit improved photocatalytic performance compared with that of pure g-C_3N_4. Among various heterojunction configurations, 2D/2D nanostructures with large interfacial contact areas are preferred[18]. Further exploration of high-performance, easy-to-prepare g-C_3N_4-

[1]Department of Blood Transfusion & Medical Research Center, The Affiliated Hospital of Qingdao University, Qingdao University, Qingdao 266003, China. [2]Immunology & Pathogenic Biology, School of Basic Medicine, Medical College, Qingdao University, Qingdao 266071, China. [3]School of Environmental Science and Engineering, State Key Laboratory of Bio-Fibers and EcoTextiles, Qingdao University, Qingdao 266071, China. [4]Ping Li and Yuting Zhai contributed equally to this manuscript. ✉email: zhangshuchao@qdu.edu.cn

based semiconducting heterojunction materials for photocatalytic sterilization applications is needed to achieve more efficient sterilization outcomes.

Two-dimensional molybdenum disulfide (MoS_2) is considered a potential high-performance metal-free cocatalyst with the following unique properties: (i) good biocompatibility[19]; (ii) tuneable energy band gap ranges from 1.2 to 1.9 eV, which increases as the thickness decreases[20]; (iii) high specific surface area, which is favourable for surface modification and drug loading[21]; and (iv) broad spectral absorption range, which enable the absorption of different bands of light to facilitate diverse applications[22]. The excellent physicochemical properties of 2D molybdenum disulfide (MoS_2) nanosheets include their high surface area, good electrical conductivity, and good surface retention, and thus, these nanosheets could be used as biocides. Molybdenum sulfide (MoS_2) is a 2D nanomaterial that has potential for biomedical applications in terms of antimicrobial activity[23]. The suitability of MoS_2 nanosheets can be attributed to their high surface area, good electrical conductivity and unique properties. In addition, since MoS_2 nanosheets can induce physical damage and lead to bacterial inactivation, they are potential antimicrobial agents against Gram-negative bacterial infections[24]. These unique properties are promising for photocatalytic applications. MoS_2 and g-C_3N_4 have similar layered structures and are more likely to form close associations; this not only reduces the lattice mismatch but also creates a new electric field-modulated electronic energy-band structure at the interface of MoS_2 and g-C_3N_4 to enhance charge transfer[25]. Thus, MoS_2 was selected as another semiconductor structure.

In this study, we synthesized an MoS_2/g-C_3N_4 photocatalyst with enhanced sterilization activity using a simple hydrothermal method. We constructed a tightly integrated layered composite structure that significantly improved the photoreduction potential, facilitating interfacial charge separation and electron transfer from g-C_3N_4 to MoS_2 and thereby promoting the overall photocatalytic reaction. The high specific surface area provided numerous reactive sites, and the shorter diffusion pathways improved the electron mobility, leading to faster photocarrier separation and transfer. Consequently, the photocatalytic performance of MoS_2/g-C_3N_4 heterojunction was markedly enhanced, and complete inactivation of *E. coli* and *S. aureus* was attained within 20 min and 30 min, respectively, under irradiation with a white LED lamp.

Experimental section

Synthesis of MoS_2

First, 0.124 g $(NH_4)_6Mo_7O_{24}\cdot 4H_2O$ and 0.22 g H_2NCSNH_2 were dissolved in 20 mL pure water. The solution was added to a Teflon-lined autoclave and allowed to react at 180 °C for 24 h. The samples were repeatedly rinsed with ethanol and deionized water before drying at 60 °C for 6 h. Cooling to room temperature, the samples were placed in an EP tube and set aside.

Synthesis of g-C_3N_4

First, 10 g of melamine was calcined in a muffle furnace at 550 °C for 2 h in air at a heating rate of $5°C min^{-1}$. The samples were kept at 550 °C for an additional 2 h. The resulting yellow powder, bulk C_3N_4, was ground into a faint-yellow powder and stored for later use. The obtained g-C_3N_4 was dispersed in 20 mL of secondary water and subjected to ultrasonication for 3 h.

Synthesis of MoS_2/g-C_3N_4 heterostructure composites

MoS_2/g-C_3N_4 layered heterojunctions were synthesized via a simple hydrothermal method. First, 20 mL of secondary water was added to 0.075 g of C_3N_4, and the mixture was ultrasonicated for 1 h. The resulting solution was added to a reactor, and the above-mentioned medicines used to synthesize MoS_2 were simultaneously placed into the reactor at 180 °C for 24 h to obtain MoS_2/g-C_3N_4 heterojunctions (mass ratio = 3:2), as depicted in Fig. 1.

Characterization

The DX2700 was operated at 40 kV and 30 mA. The pure MoS_2, pure g-C_3N_4, and g-C_3N_4/MoS_2 photocatalysts were analysed using X-ray diffraction with Cu Kα radiation ($\lambda = 1.5418$ Å) to characterize the crystalline nature of the materials. The morphology of the samples was examined using an FEI Magellan 400 scanning electron microscope and a JEOL JEM-2100 F and Tecnai G2 F20 America FEI transmission electron microscope. Raman spectra were measured with a Thermo Scientific DXR2 using an excitation wavelength of 532 nm. The structures of the photocatalysts were analysed using the Brunauer–Emmett–Teller (BET) method via the 3 H-2000PS2 static volume technique. X-ray photoelectron spectroscopy (XPS) using Thermo ESCELAB 250XI Thermo America detection. Fourier Transform Infrared (FTIR) detection using Nicolet is50. High Sensitivity Zeta Potential and Particle Size Analyser 90PluSPALS Detects Zeta Potential and Particle Size.

Photocatalytic bacterial inactivation experiments

Gram-negative *Escherichia coli* (*E. coli*) and Gram-positive *Staphylococcus aureus* (*S. aureus*) were used to evaluate the photocatalytic antimicrobial activity of the prepared MoS_2/g-C_3N_4 heterojunctions. First, 20 mg of the material was added to 20 mL of ultrapure water to prepare a 1 mg/mL suspension; this suspension was then subjected to high-pressure sterilization for future use. The bacterial cells were added to the suspension to achieve a final cell density of approximately 1.0×10^7 colony-forming units (CFUs) per mL. The suspension was then exposed to a white LED light source (100 W, 50 mW/cm^2) for irradiation. Prior to irradiation, the suspension was stirred in the dark for 30 min to fully mix the material with the bacterial solution. The circulating water was cooled to maintain room temperature (20 °C) during the reaction. During the irradiation process, samples were collected at different times. Specifically, 100 μL of the reaction solution was taken from the reactor, serially diluted five times with ultrapure water, and inoculated onto nutrient agar plates. The Petri dishes were then placed in a constant-temperature incubator at 37 °C for 24 h for colony counting. After 24 h, the colonies were counted, and the average number of colonies was calculated from three replicates. Fluorescence images of the

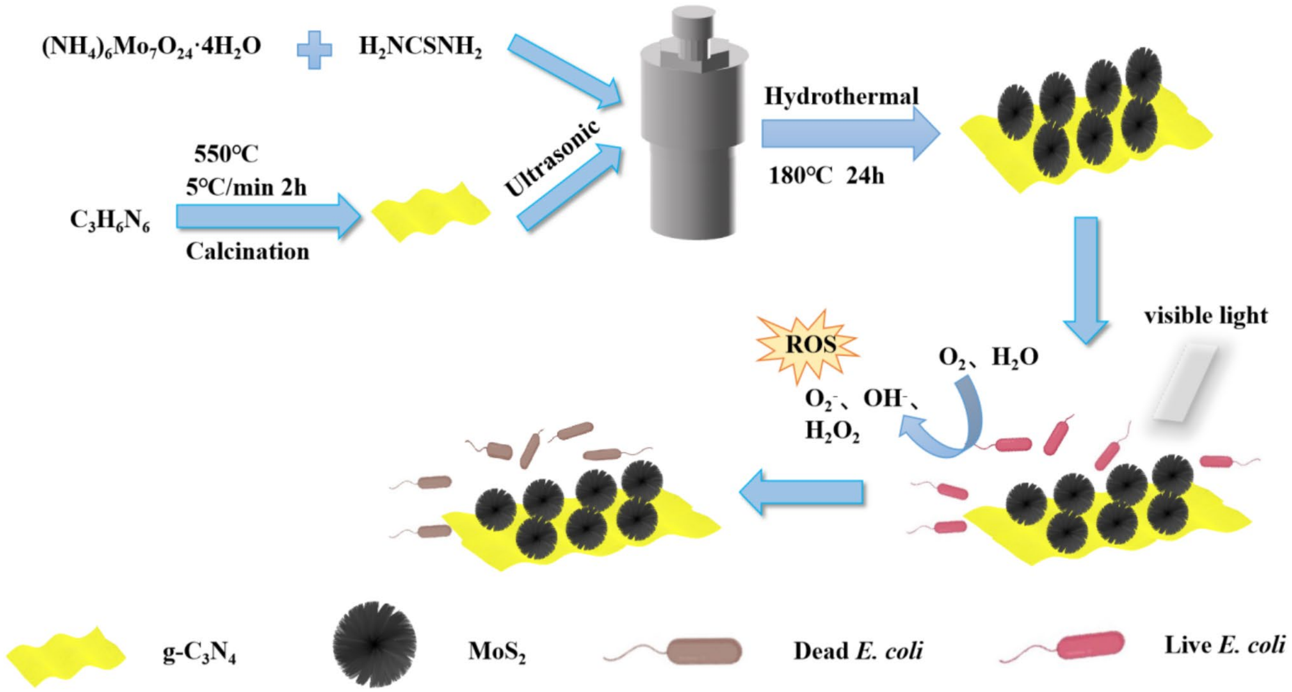

Fig. 1. Synthesis and antimicrobial effects of the g-C_3N_4/MoS_2.

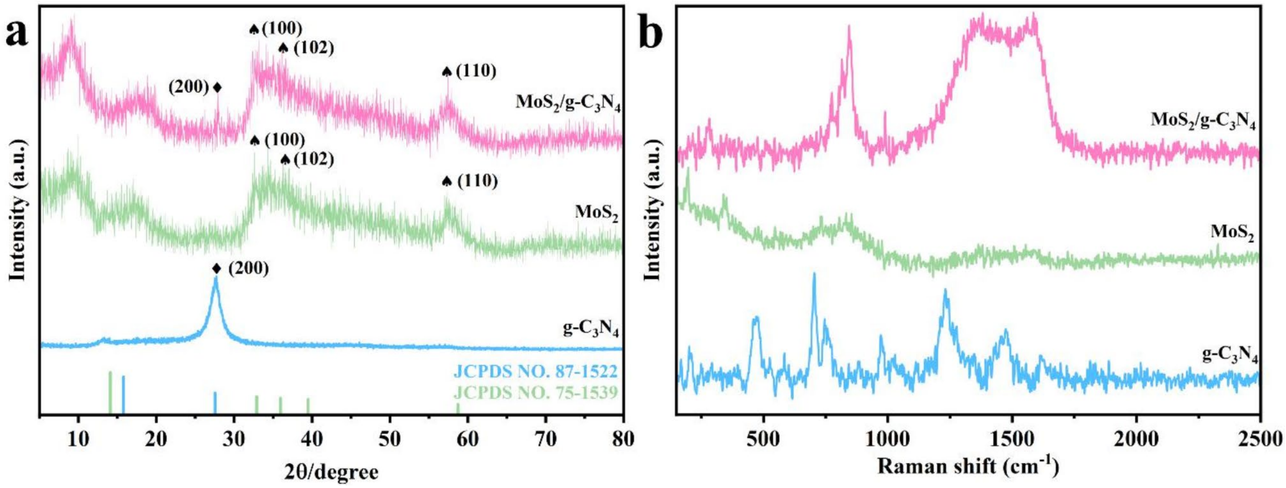

Fig. 2. (**a**) XRD diffraction patterns and (**b**) Raman spectra of various samples.

bacterial cells were acquired using a confocal laser scanning microscope (Leica SPE) with Syto 9 and propidium iodide as fluorescent dyes. An appropriate amount of the ROS scavenger was added to the 5 mL mixed system of material and bacterial suspension, the mixture was reacted for the same amount of time under light, and the changes in the number of colonies were observed to investigate which specific ROS scavenger acts as an antimicrobial agent.

Results and discussion

Characterization of MoS_2/g-C_3N_4

The X-ray diffraction (XRD) patterns of the prepared samples are shown in Fig. 2a. The diffraction peak of g-C_3N_4 at 27.4° corresponds to the (200) crystal plane (JCPDS NO. 87-1522)[26]. The diffraction peaks of MoS_2 at 32.9° and 57.7° correspond to the (100) and (110) crystal planes, respectively (JCPDS NO. 75-1539)[27]. Moreover, in the MoS_2/g-C_3N_4 heterojunction material, the coexisting (200) crystal planes of g-C_3N_4 and the (100) and

(110) crystal planes of MoS_2 are clearly observed. These results confirm that the heterojunction material was successfully synthesized and that the structure of each component remained stable during the preparation and composite processes, providing a basis for heterojunction formation.

The Raman spectra of the different samples are shown in Fig. 2b. Pure g-C_3N_4 exhibits two Raman peaks at 1352 cm^{-1} and 1596 cm^{-1}; these correspond to the characteristic D and G peaks, respectively, of the g-C_3N_4 graphitic material[28]. Pure MoS_2 displays two peaks at 380.3 cm^{-1} and 407.8 cm^{-1}; these peaks are attributed to the in-plane ($E^1{}_{2g}$) and out-of-plane (A_{1g}) vibrational modes, respectively[29]. The MoS_2/g-C_3N_4 composite also shows distinct D and G peaks along with two MoS_2 bands; these results indicate that the structures of all components within the composite remain intact. These results further confirm the successful synthesis of the composite sample and are consistent with the XRD results. FTIR spectra (Fig. S1) similarly indicate the successful synthesis of MoS_2/g-C_3N_4 composites. Peaks of 749 cm^{-1} from MoS_2 and 2986 cm^{-1} from g-C_3N_4 can be observed on the composite.

Scanning electron microscopy (SEM) and transmission electron microscopy (TEM) images of each prepared sample are shown in Fig. 3. Figure 3a shows an SEM image of the prepared pure MoS_2; here, the image reveals a microspherical shape that is fluffy, porous, and free of agglomeration. The TEM image of MoS_2 is shown in Fig. S4. Figure 3b presents an SEM image of pure g-C_3N_4, and a lamellar stacking structure is clearly observed. The SEM image of the composite sample MoS_2/g-C_3N_4 is shown in Fig. 3c; here, the layers of lamellar g-C_3N_4 are attached to the surface of the spherical MoS_2. Figure 3d shows a TEM image of pure MoS_2, in which the spherical three-dimensional MoS_2 appears as a black shaded portion due to its resistance to electron penetration. Figure 3e shows a TEM image of pure g-C_3N_4; here, the image reveals distinct multilayered lamellar stacking, and this result is consistent with the SEM results. Figure 3f shows the TEM image of the composite sample MoS_2/g-C_3N_4; in this image, the multilayer lamellar g-C_3N_4 is anchored around the spherical MoS_2, and this confirms the successful synthesis of the composite material and the formation of a heterogeneous structure.

The nitrogen adsorption/desorption isothermal curves of each prepared material are shown in Fig. 4a. The isotherms of the three materials exhibit inflection points in the low-pressure region. In the high-pressure region, the adsorption and desorption curves do not overlap, displaying evident hysteresis loops, indicative of a clear Type IV curve. The specific surface areas of MoS_2, g-C_3N_4 and MoS_2/g-C_3N_4 are 166.36, 43.69 and 107.96 m^2/g, respectively. The pore size distributions of the three samples shown in Fig. 4b reveal that the pore sizes of all three materials are in the range of 2–50 nm; these results indicate a standard mesoporous structure and are consistent with the H1 hysteresis loop observed in the adsorption/desorption isotherms. The pore size distributions of MoS_2, g-C_3N_4, and $MoS_{2/}$g-C_3N_4 are 11.26, 16.55, and 12.63 nm, respectively. The composites combine the large specific surface area of MoS_2 with the large pore size of g-C_3N_4 to provide extensive reactive sites for the catalytic reactions.

X-ray photoelectron spectroscopy (XPS) results confirm the successful synthesis of MoS_2/g-C_3N_4 composites (Fig. S3). The characteristic peaks of Mo 3d, C 1s, N 1s and S 2p orbitals observed in the composites proved the effective combination of the two components. The XPS spectra in the Mo 3d region, two different peaks were observed at the BE of 228.5 and 231.8 eV. In the XPS spectra of the S 2p region, two distinct main peaks are observed at BE of 161.6 and 162.7 eV. Notably, the binding energy shifts of Mo 3d at 231.8 eV and 228.5 eV indicate that the electronic structure of MoS_2 changes significantly when interacting with g-C_3N_4, which suggests

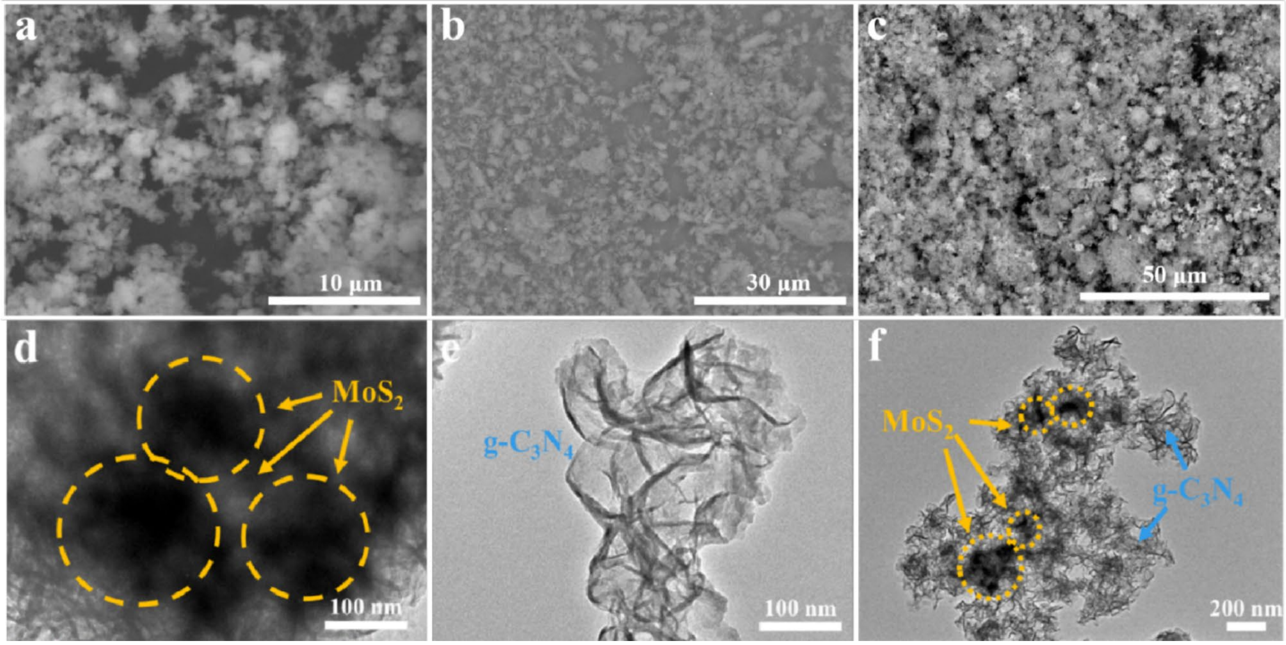

Fig. 3. SEM images of pure MoS_2(**a**), g-C_3N_4 (**b**), MoS_2/g-C_3N_4 (**c**) and TEM images of MoS_2 (**d**), g-C_3N_4 (**e**), MoS_2/g-C_3N_4 (**f**).

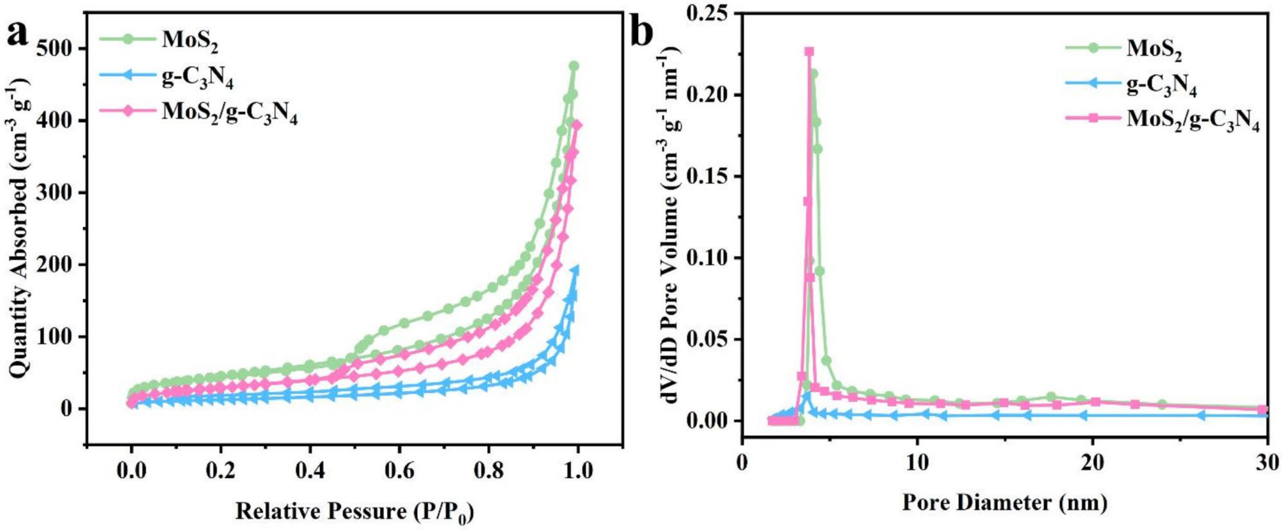

Fig. 4. (**a**) Nitrogen adsorption and desorption isotherms of MoS_2, g-C_3N_4 and MoS2/g-C_3N_4 and (**b**) pore size distributions.

that there is a strong chemical bond between the two materials[30]. The spectrum of the C 1s region of the pure g-C_3N_4, MoS_2/g-C_3N_4 sample exhibit two major peaks at BEs of 284.5 eV (attributed to reference C atoms) and 285.9 eV (attributed to C sp2-hybridized atoms of the terminal $C(N)_3$ structure in tri-s-triazine aromatic units)[31]. The high-resolution XPS spectrum of the pristine g-C_3N_4 N1s region shows two peaks located at BEs of 398.7 eV and 400.8 eV, which can be indexed to the nitrogen atoms in C=N-C and -NH_2 bonds, respectively[32].

The results presented in Fig. S6 highlight important insights into the physicochemical properties of MoS_2 and g-C_3N_4, as well as their composite MoS_2/g-C_3N_4. Zeta potential measurements (Fig. S6a) indicate that MoS_2/g-C_3N_4 composites present a distinctive waveforms, suggesting the existence of synergistic interactions between the components, which may enhance their electrochemical properties. In the corresponding hydrodynamic diameter analysis (Fig. S6b), the average diameter of MoS_2 (1087.58 nm) is significantly larger than that of the composite (429.93 nm) and g-C_3N_4 (583.37 nm). The narrower distribution observed in the composites indicates improved dispersion, which contributes to better contact with the bacterial fluid in practical applications.

Photocatalytic antibacterial properties of MoS_2/g-C_3N_4

Firstly, the look antimicrobial function of the composites with different ratios was done by pre-experiment as shown in Fig. S2, the results showed that MoS_2/g-C_3N_4 (3:1) has more toxicity than MoS_2/g-C_3N_4 (3:2) under dark condition for 30 min. Therefore, MoS_2/g-C_3N_4 (3:2) was chosen for the subsequent experiments. The photocatalytic bacterial inactivation activity of the synthesized MoS_2/g-C_3N_4 heterostructures was evaluated using *E. coli* and *S. aureus*. Notably, almost no bacterial inactivation was observed in the dark (dark control) or under light irradiation without photocatalysts (light control) for either *E. coli* or *S. aureus*. The bare C_3N_4 exhibited negligible bactericidal efficiency under white LED light irradiation. Impressively, the addition of MoS_2/g-C_3N_4 or MoS_2, both of which have broader visible light absorption, significantly enhanced photocatalytic antibacterial activity, especially the MoS_2/g-C_3N_4 heterostructure. As shown in Fig. 5a-b, in the spread plate assays, no visible colonies were observed in the MoS_2/g-C_3N_4 group after 30 min of irradiation under LED light. The improved photocatalytic performance compared with that of the pure MoS_2 group indicates that the formation of heterogeneous structures promotes photocatalysis. Moreover, the antibacterial rate towards *E. coli* (Fig. 6a) was slightly greater than that towards *S. aureus* (Fig. 6b) because of the differences in cell wall structure.

The durability of a photocatalyst across multiple antimicrobial cycles is crucial for practical water disinfection. As shown in Fig. 6c, E. *coli* was completely inactivated within three antimicrobial cycles, each lasting 30 min. Although the antimicrobial resistance slightly decreased in the fourth and fifth cycles, it remained significant. These results highlight the high stability and robustness of MoS_2/g-C_3N_4 in the photocatalytic inactivation of bacteria.

To determine the primary reactive species for photocatalytic bacterial inactivation, the scavenger used by Zhang et al. was selected[33]. Various scavengers have been introduced into the system: Cr(VI) for electrons (e^-), isopropanol for hydroxyl radicals (·OH), sodium oxalate for holes (h^+), 4-hydroxy-2,2,6,6-tetramethylpiperidinyloxy (TEMPO) for superoxide radicals ($\cdot O_2^-$), and catalase for hydrogen peroxide (H_2O_2)[34,35]. As shown in Fig. 6d, the addition of Cr(VI) to capture e^- significantly reduced the photocatalytic antibacterial activity, and no antibacterial activity was observed; these results indicated that the enhancement was primarily due to the improved separation efficiency of photogenerated e^-–h^+. The slight decrease in antibacterial activity upon the addition of isopropanol indicated that ·OH played a minor role. The pronounced inhibition of bacterial inactivation observed with the addition of sodium oxalate, TEMPO, and catalase indicated that h^+, $\cdot O_2^-$, and H_2O_2 were crucial species for photocatalytic antibacterial activity, particularly active H_2O_2.

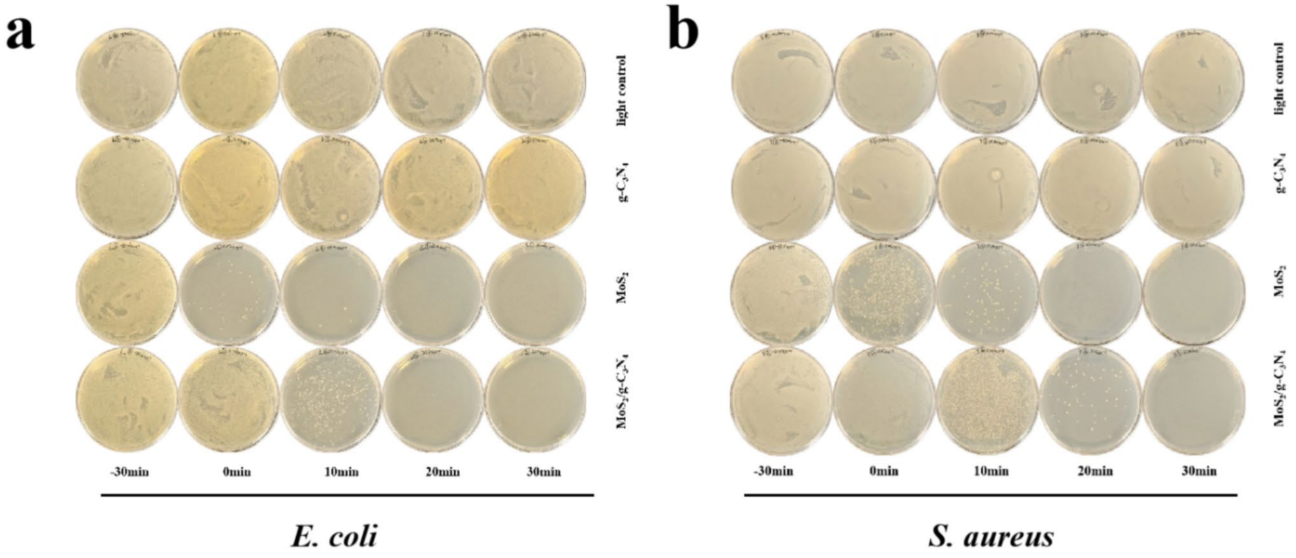

Fig. 5. Photocatalytic performance of MoS_2/g-C_3N_4 against *E. coli* (**a**) and *S. aureus* (**b**).

As shown in Fig. 7, the red and green fluorescence in the stained cell images indicate dead and live *S. aureus*, respectively. Without visible light irradiation, the bacteria clearly exhibited green fluorescence with minimal red fluorescence, indicating that many bacteria survived. Upon visible light irradiation, the images displayed red fluorescence, indicating the death of all the *Staphylococcus aureus* bacteria. Thus, this heterogeneous structure has a photocatalytic sterilization effect.

As shown in Fig. S5, the composite MoS_2/g-C_3N_4 has good biocompatibility, which was achieved by haemolysis experiments, and the haemolysis rates of pure MoS_2, g-C_3N_4 and MoS_2/g-C_3N_4 were all under 3%, which demonstrated its biosafety.

Photocatalytic activity enhancement mechanism of MoS_2/g-C_3N_4

Figure 8 shows the mechanism underlying the enhanced photocatalytic performance of the synthesized MoS_2/g-C_3N_4 heterostructures. As shown in the left panel of Fig. 8a, the work functions (WFs) of MoS_2 and g-C_3N_4 are calculated from the Ultraviolet Photoelectron Spectroscopy (UPS) data and are 2.74 eV and 5.15 eV, respectively. The work function of MoS_2 is much lower, and MoS_2 acts as an electron transfer channel to attain efficient charge transfer. The right figure shows the Fermi edge of the sample; here, the valence band top of the sample can be derived, the valence band (VB) of the sample can be derived by the conversion of the vacuum energy level, and the valence bands of MoS_2 and g-C_3N_4 are 1.85 eV and 3.07 eV, respectively. The Mott Schottky curve of the sample is shown in Fig. 8b; thus, MoS_2 is an n-type semiconductor, the tangent slope of the M-S curve is positive, and the flat band potential E_{FB} is -0.36 eV, and its conduction band E_{CB} is approximately – 0.36 eV - (0.1–0.3 eV). Additionally, g-C_3N_4 has a negative M-S curve tangent slope and is a p-type heterojunction, and the flat-band potential E_{FB} is 0.22 eV; this value indicates that the conduction band of g-C_3N_4 is approximately 0.22 eV + (0.1–0.3 eV). Figure 8c shows that the band gap of g-C_3N_4 (Eg) of g-C_3N_4 is 2.62 eV, and its conduction band is 0.45 eV from Eq. (1); these results are consistent with the deduction from the Mott Schottky results. Since MoS_2 is a black material, its UV-vis diffuse reflection is difficult to attain; thus, the approximate position of the conduction band of MoS_2 is derived from the M-S curve to further explore its photocatalytic performance. Under white LED light irradiation, MoS_2 generates photogenerated electron-hole pairs, where electrons are excited from the valence band to the conduction band, and holes remain in the valence band. The electrons migrate from MoS_2 to g-C_3N_4, whereas the holes move from g-C_3N_4 to MoS_2; thus, carrier recombination is prevented, and the photocatalytic activity is significantly enhanced. During the photocatalytic antimicrobial process, $\cdot O_2^-$ radicals and H_2O_2, produced by the reaction of electrons with O_2 and H_2O, play crucial roles in the sterilization process[36], as shown in Eq. (2).

$$E_{VB} = E_{CB} + E_g. \tag{1}$$

$$e^- + O_2 \rightarrow \cdot O_2^- + H_2O \rightarrow H_2O_2. \tag{2}$$

Conclusion

In summary, the MoS_2/g-C_3N_4 heterostructure synthesized via a simple hydrothermal method exhibits enhanced photocatalytic performance and effectively eliminated *E. coli* and *S. aureus* within 20 min under irradiation with a white LED lamp. This significant increase in photocatalytic activity is attributed to the ability of the nanoheterostructure to reduce the recombination of the photogenerated electron-hole pairs and enhance the carrier transport; thus, the production of reactive oxygen species (h^+, $\cdot O_2^-$, and H_2O_2) was enhanced. This work

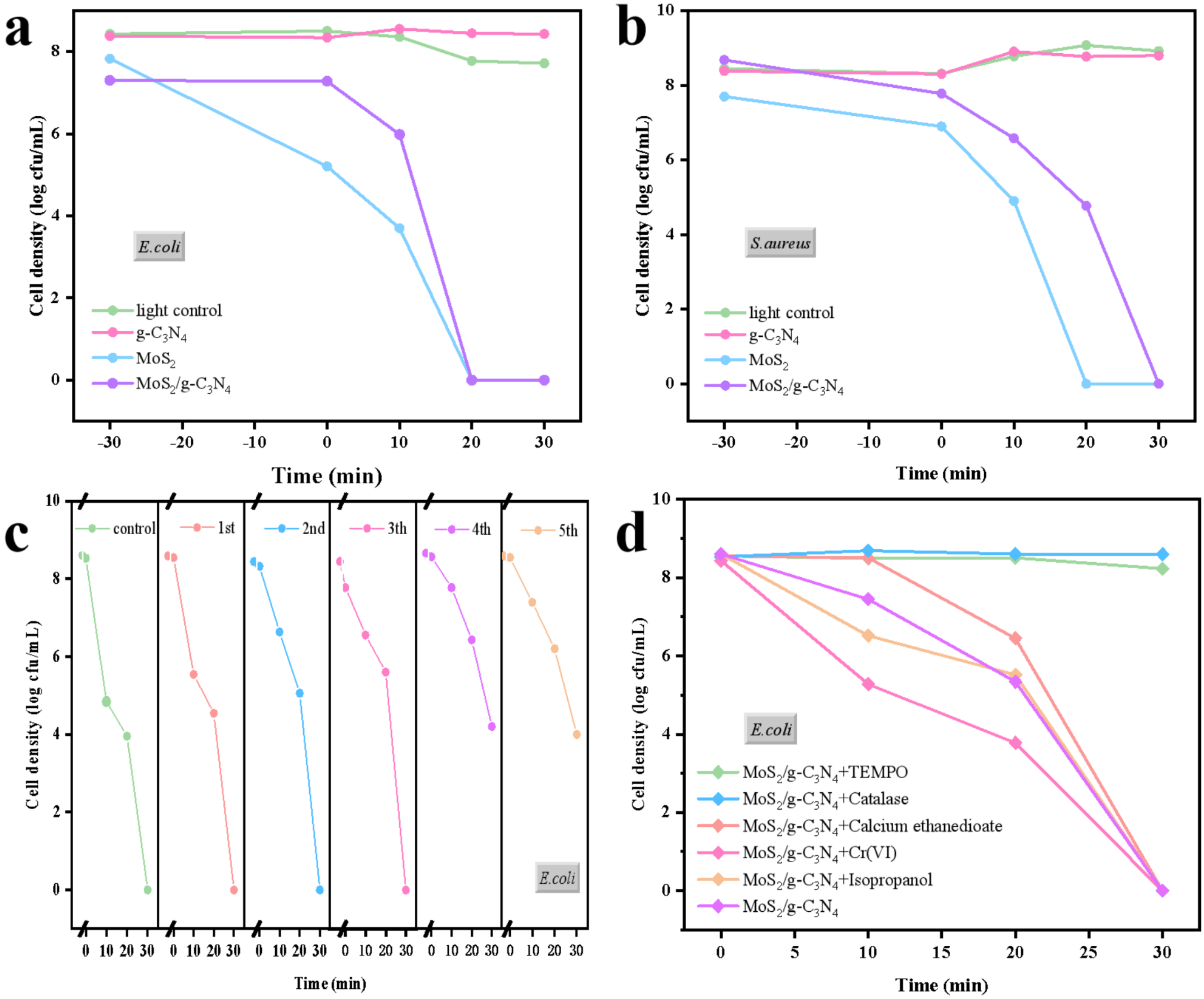

Fig. 6. Photocatalytic antibacterial activity of $MoS_2/g\text{-}C_3N_4$ heterostructure under white LED light irradiation and control experiments. The inactivation performances against *E. coli* (**a**) and *S. aureus* (**b**) and the corresponding spread plate results of *E. coli* and *S. aureus*, respectively. (**c**) Recycling experiments of photocatalytic inactivation of *E. coli* over $MoS_2/g\text{-}C_3N_4$. (**d**) Photocatalytic antibacterial activity of $MoS_2/g\text{-}C_3N_4$ in the presence of different scavengers under white LED irradiation.

introduces a novel photocatalyst for LED photocatalytic water purification, thereby expanding the applications of photocatalytic antibacterial technologies.

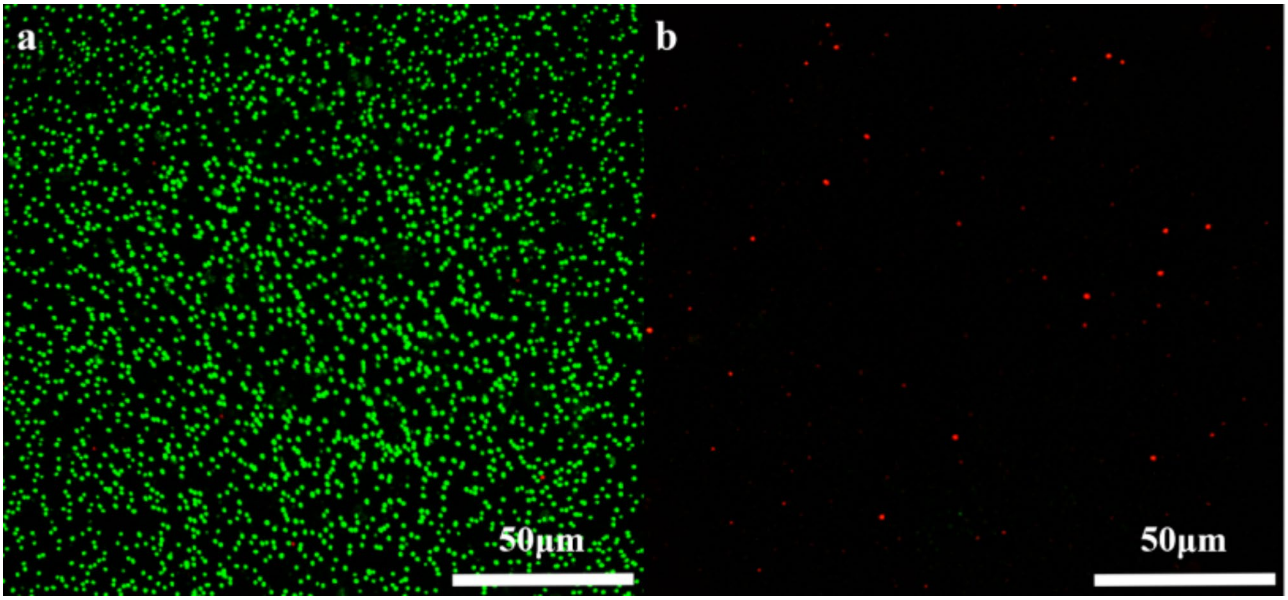

Fig. 7. Merged fluorescence-stained images of *S. aureus*; green and red indicate live and dead *S. aureus*, respectively.

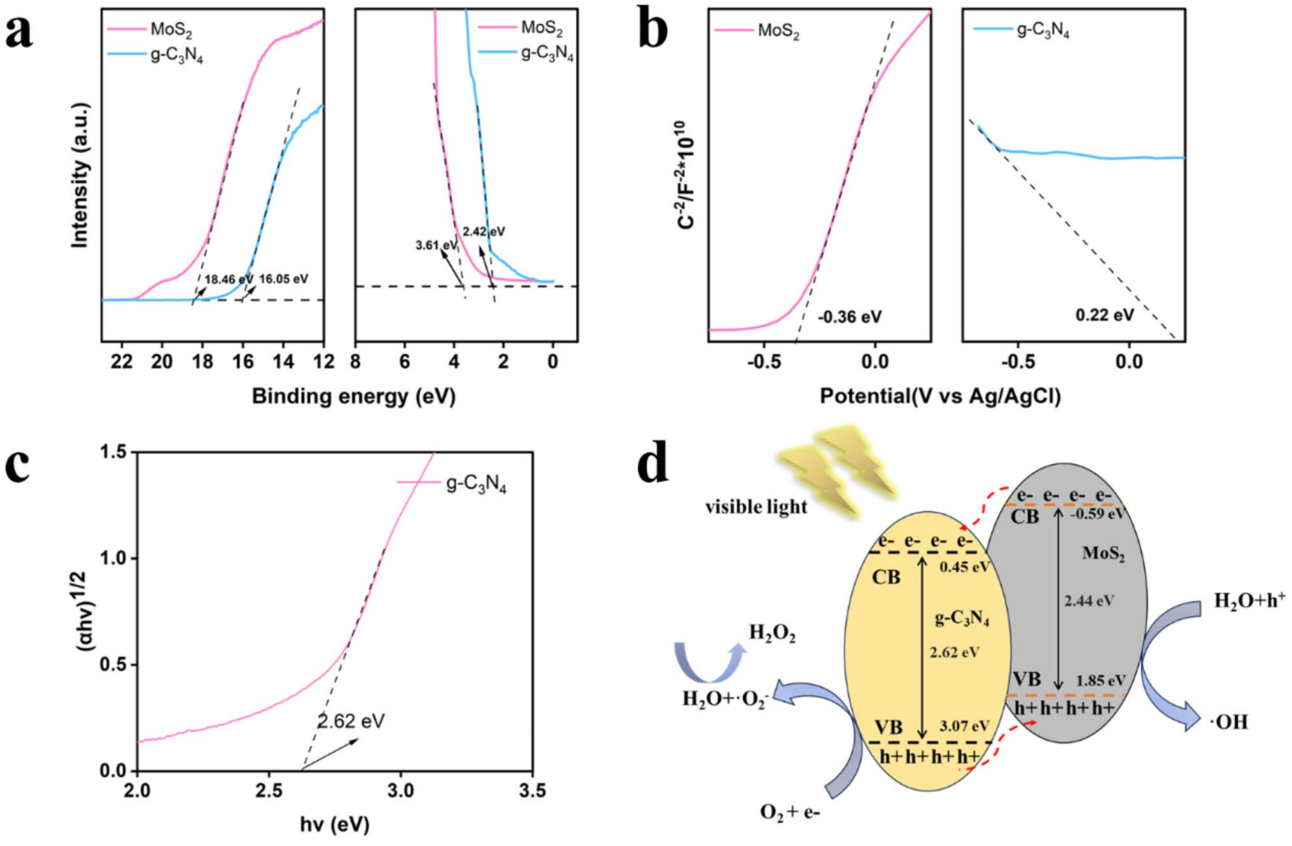

Fig. 8. (**a**) Tauc plots and work functions of MoS_2 and g-C_3N_4, (**b**) Mott–Schottky plots, (**c**) UV–Vis diffuse reflectance spectra, and (**d**) proposed mechanism for the photocatalytic bacterial inactivation by MoS_2/g-C_3N_4.

Data availability

All data generated or analysed during this study are included in this published article.

Received: 15 October 2024; Accepted: 7 March 2025

References

1. Shivaram, K. B., Bhatt, P., Verma, M. S., Clase, K. & Simsek, H. Bacteriophage-based biosensors for detection of pathogenic microbes in wastewater. *Sci. Total Environ.* **901**, 18 (2023).
2. Karwowska, B. & Sperczynska, E. Coagulation enhanced with adsorption and ozonation processes in surface water treatment. *Sustainability* **15**, 15 (2023).
3. Samsudin, M. F. R., Sufian, S. & Hameed, B. H. Epigrammatic progress and perspective on the photocatalytic properties of $BiVO_4$-based photocatalyst in photocatalytic water treatment technology: A review. *J. Mol. Liq.* **268**, 438–459 (2018).
4. Zhou, Z. L. et al. Recent progress in photocatalytic antibacterial. *ACS Appl. Bio Mater.* **4**, 3909–3936 (2021).
5. Popova, A. et al. Synergistic bactericidal effect of Zn^{2+} ions and reactive oxygen species generated in response to either UV or X-ray irradiation of Zn-Doped plasma electrolytic oxidation TiO_2 coatings. *Acs Appl. Bio Mater.* **7**, 5579–5596 (2024).
6. Baamer, D. F., Helmy, E. T., Mostafa, M. M. M. & Pan, J. H. Synthesis of TiO_2 nanoparticles using different routes with enhanced photocatalytic and antibacterial properties. *Ceram. Int.* **50**, 15780–15789 (2024).
7. Bao, T. et al. Recent advances of graphitic carbon nitride (g-C_3N_4) based materials for photocatalytic applications: A review. *Nano Mater. Sci.* (2024).
8. Qi, K., Cheng, B., Yu, J. & Ho, W. Review on the improvement of the photocatalytic and antibacterial activities of ZnO. *J. Alloys Compd.* **727**, 792–820 (2017).
9. Yang, Y., Guan, C. L. & Chen, S. Y. Structural characterization and catalytic sterilization performance of a TiO_2 nano-photocatalyst. *Food Sci. Nutr.* **8**, 3638–3646 (2020).
10. Du, Y. H. et al. Metal free benzothiadiazole-diketopyrrolopyrrole-based conjugated polymer/g-C_3N_4 photocatalyst for enhanced sterilization and degradation in visible to near-infrared region. *J. Colloid Interf Sci.* **608**, 103–113 (2022).
11. Jin, C. et al. Enhanced photocatalytic antibacterial performance by hierarchical TiO_2/W_8O_{49} Z-scheme heterojunction with $Ti_3C_2T_x$-MXene Cocatalyst. *Chem. Eng. J.* **447** (2022).
12. Khatami, M. & Iravani, S. Green and Eco-Friendly synthesis of nanophotocatalysts: an overview. *Comment Inorg. Chem.* **41**, 133–187 (2021).
13. Wu, X. H., Tan, L. H., Chen, G. Q., Kang, J. Y. & Wang, G. H. g-C_3N_4-based S-scheme heterojunction photocatalysts. *Sci. China-Mater*. **67**, 444–472 (2024).
14. Muhmood, T. et al. Graphene-like graphitic carbon nitride (g-C_3N_4) as a semiconductor photocatalyst: properties, classification, and defects engineering approaches. *Mater. Today Sustain.* **25**, 20 (2024).
15. Ma, X. J. et al. Mechano-synthesized TiO_2/g-C_3N_4 composites for rapid photocatalytic removal of perrhenate. *J. Environ. Chem. Eng.* **11**, 10 (2023).
16. Ding, F. et al. Bi_2MoO_6/g-C_3N_4 of 0D/2D heterostructure as efficient photocatalyst for selective oxidation of aromatic alkanes. *Appl. Surf. Sci.* **490**, 102–108 (2019).
17. Yin, Y. Y. et al. Unique $BiFeO_3$/g-C_3N_4 mushroom heterojunction with photocatalytic antibacterial and wound therapeutic activity. *Nanoscale* **14**, 2686–2695 (2022).
18. Sun, Z. C. et al. Construction of 2D/2D $BiVO_4$/g-C_3N_4 nanosheet heterostructures with improved photocatalytic activity. *J. Colloid Interface Sci.* **533**, 251–258 (2019).
19. Kaushik, R., Nandi, S., Mandal, M. & Gupta, A. N. Biocompatible I-Cysteine-Capped MoS_2 nanoflowers for antibacterial applications: mechanistic insights. *Acs Appl. Nano Mater.* **7**, 7753–7765 (2024).
20. Na, J. et al. Indirect band gap in scrolled MoS_2 monolayers. *Nanomaterials* **12**, 10 (2022).
21. Qi, X. T., Ye, P. K. & Xie, M. MoS_2 quantum Dots based on lipid drug delivery system for combined therapy against Alzheimer?s disease. *J. Drug Deliv Sci. Technol.* **82**, 11 (2023).
22. Singh, A. et al. Near-infrared optical properties and proposed phase-change usefulness of transition metal disulfides. *Appl. Phys. Lett.* **115**, 5 (2019).
23. Dharmalingam, K. et al. Novel MoS_2-In_2O_3-WS_2 (2D/3D/2D) ternary heterostructure nanocomposite material: efficient photocatalytic degradation of antimicrobial agents under visible-light. *Environ. Res.* **261** (2024).
24. Liang, J. et al. Lignin-ultrasound method: enhancement of antimicrobial capacity of MoS_2-containing films. *Int. J. Biol. Macromol.* **252** (2023).
25. Senthilnathan, S. et al. MoS_2 modified g-C_3N_4 composite: A potential candidate for photocatalytic applications. *J. Saudi Chem. Soc.* **27**, 10 (2023).
26. Zhu, Z. et al. Fabrication of graphene modified CeO_2/g-C_3N_4 heterostructures for photocatalytic degradation of organic pollutants. *Chin. J. Struct. Chem.* **42**, 8 (2023).
27. Chen, H. Z. et al. A first-principles study on the hydrodeoxygenation mechanism of the lignin-derived phenolic compounds over MoS_2 catalysts. *Ind. Crop Prod.* **214**, 13 (2024).
28. Jiang, J. et al. Dependence of electronic structure of g-C_3N_4 on the layer number of its nanosheets: A study by Raman spectroscopy coupled with first-principles calculations. *Carbon* **80**, 213–221 (2014).
29. Tan, C. K. et al. Raman studies of MoS_2 under strain at different uniaxial directions. *Vacuum* **153**, 274–276 (2018).
30. Yanalak, G. et al. Transition metal (Ni, co)-doped graphitic carbon nitride/MoS_2 heterojunctions as efficient photocatalysts for hydrogen evolution reaction under visible light. *Int. J. Energy Res.* **46**, 17189–17203 (2022).
31. Eroglu, Z. & Metin, O. Internal interactions within the complex Type-II heterojunction of a graphitic carbon nitride/black phosphorus hybrid decorated with graphene quantum Dots: implications for photooxidation performance. *ACS Appl. Nano Mater.* **6**, 7960–7974 (2023).
32. Chen, J. et al. Red phosphorus Nanodot-Decorated polymeric carbon nitride nanotubes for Visible-Light-Driven photocatalytic bacterial inactivation. *ACS Appl. Nano Mater.* **5**, 862–870 (2022).
33. Acar, E. G. et al. Solar-light-driven photocatalytic hydrogen evolution activity of gCN/WS2 heterojunctions incorporated with the first-row transition metals. *J. Alloys Compd.* **950**, 11 (2023).
34. Liu, J. X. et al. Visible-light driven rapid bacterial inactivation on red phosphorus/titanium oxide nanofiber heterostructures. *J. Hazard. Mater.* **413**, 9 (2021).
35. He, D. Y. et al. Black phosphorus/graphitic carbon nitride: A metal-free photocatalyst for green photocatalytic bacterial inactivation under visible light. *Chem. Eng. J.* **384** (2020).
36. Pan, C. S. et al. Efficient and stable H_2O_2 production from H_2O and O_2 on $BiPO_4$ photocatalyst. *Appl. Catal. B-Environ.* **316** (2022).

Acknowledgements

The authors are grateful for the financial support from a grant from the Scientific Research Programs of the International Association of Asia–Pacific Blood Types and Genomics (Grant No. IAABG23SR004), and Shandong Province Medicine and Health Science and Technology Project (Grant No. 202411000745).

Author contributions

P.L. and Y.Z. wrote the main manuscript text; J.L. experimented; Y.D. and D.L. were responsible for data analysis; S.Z. was responsible for editing and supervision; all authors contributed to the general discussion.

Declarations

Competing interests

The authors declare no competing interests.

Additional information

Supplementary Information The online version contains supplementary material available at https://doi.org/10.1038/s41598-025-93489-1.

Correspondence and requests for materials should be addressed to S.Z.

Reprints and permissions information is available at www.nature.com/reprints.

Publisher's note Springer Nature remains neutral with regard to jurisdictional claims in published maps and institutional affiliations.

Open Access This article is licensed under a Creative Commons Attribution-NonCommercial-NoDerivatives 4.0 International License, which permits any non-commercial use, sharing, distribution and reproduction in any medium or format, as long as you give appropriate credit to the original author(s) and the source, provide a link to the Creative Commons licence, and indicate if you modified the licensed material. You do not have permission under this licence to share adapted material derived from this article or parts of it. The images or other third party material in this article are included in the article's Creative Commons licence, unless indicated otherwise in a credit line to the material. If material is not included in the article's Creative Commons licence and your intended use is not permitted by statutory regulation or exceeds the permitted use, you will need to obtain permission directly from the copyright holder. To view a copy of this licence, visit http://creativecommons.org/licenses/by-nc-nd/4.0/.

© The Author(s) 2025